Development of a laser photothermoacoustic frequency-swept system for subsurface imaging: Theory and experiment

Ying Fan and Andreas Mandelis
Center for Advanced Diffusion-Wave Technologies, Department of Mechanical and Industrial Engineering, 5 King's College Road, University of Toronto, Toronto M5S 3G8, Canada

Gloria Spirou
Department of Medical Biophysics, University of Toronto and Ontario Cancer Institute/Princess Margaret Hospital, 610 University Ave, Toronto M5G 2M9, Canada

I. Alex Vitkin
Department of Radiation Oncology, University of Toronto and Ontario Cancer Institute/Princess Margaret Hospital/University Health Network, 610 University Ave, Toronto M5G 2M9, Canada

(Received 23 April 2004; revised 28 September 2004; accepted 29 September 2004)

In conventional biomedical photoacoustic imaging systems, a pulsed laser is used to generate time-of-flight acoustic information of the subsurface features. This paper reports the theoretical and experimental development of a new frequency-domain (FD) photo-thermo-acoustic (PTA) principle featuring frequency sweep (chirp) and heterodyne modulation and lock-in detection of a continuous-wave laser source at 1064 nm wavelength. PTA imaging is a promising new technique which is being developed to detect tumor masses in turbid biological tissue. Owing to the linear relationship between the depth of acoustic signal generation and the delay time of signal arrival to the transducer, information specific to a particular depth can be associated with a particular frequency in the chirp signal. Scanning laser modulation with a linear frequency sweep method preserves the depth-to-delay time linearity and recovers FD-PTA signals from a range of depths. Preliminary results performed on rubber samples and solid tissue phantoms indicate that the FD-PTA technique has the potential to be a reliable tool for biomedical depth-profilometric imaging. © *2004 Acoustical Society of America.* [DOI: 10.1121/1.1819393]

PACS numbers: 43.60.Lq, 43.80.Vj, 43.80.Qf [YHB] Pages: 3523–3533

I. INTRODUCTION

The photoacoustic (PA), or more precisely, photo-thermo-acoustic (PTA) effect, is the process of light being absorbed by a material, creating a temperature change followed by a localized volume expansion leading to the generation of acoustic waves. In addition to obvious applications in the area of subsurface depth profilometry of defects in materials,[1] there have been many advances in applying photoacoustic monitoring to soft tissue imaging, cancerous lesion detection, and subdermal depth profilometry in the last decade. In recent years, the field of laser optoacoustic (or photoacoustic) applications to biomedical imaging has enjoyed very rapid development,[2–4] becoming the object of broader attention by the biophotonics community.[5] This is so because PA detection has shown concrete promise of depth profilometric imaging in turbid media at depths significantly larger than accessible by purely optical methodologies.[6] In state-of-the-art laser PA instrumentation and measurement systems in turbid media, as developed by some of the major research groups in this field,[6–10] pulsed lasers have always been the PA signal source of choice. The major reasons for this choice are twofold: (a) Following optical absorption of a short laser pulse by turbid tissue, optical-to-thermal energy conversion and localized PTA volume expansion detection, the acoustic propagation received within approximately 1 μs after the end of the laser pulse is essentially thermally adiabatic: it carries information about the thermal shape of the absorber, which substantially coincides with its geometric shape before any significant heat conduction can deform the image at later times;[11] (b) In pulsed photoacoustics a large amount of the available energy is imparted to the Fourier spectral components of the PTA signal response, which correspond to the early times (or high frequencies) after the arrival of the acoustic pulse at the transducer, thus yielding acceptable signal-to-noise ratios under coadded transient pulse detection.[12] Pulsed PTA detection, however, presents disadvantages in terms of laser jitter noise, acoustic and thermal noise within the wide bandwidth of the transducer, easy-to-miss nascent factors of contrast-generating subsurface features amidst the series of stronger acoustic reflections for other neighboring structural inhomogeneities and boundaries, as well as strong background signals from sound-scattering tissue. These mechanisms tend to limit system detectivity and signal-to-noise ratio (SNR) and construe important limitations because they may seriously compromise the contributions to the signal of contrast-generating subsurface features and thus limit the ability to monitor nascent and small-size tumors by the PTA process. In addition, very large pulsed-laser peak irradiances incident on living tissue may have detrimental effects, and for this reason very low average pulse energies (<5 mJ) are used at the expense of SNR. Besides, it is difficult to construct linear, low-noise detection systems for a wide range of pulsed amplitudes, a common requirement for patient-specific diagnostics. Nor-

mally, acoustic responses from turbid media are time gated and Fourier transformed into the frequency domain in order to determine and match the peak response of the transducer with the frequency contents of the PTA signal.[13] Quantitatively, tissue inhomogeneity parameter measurements are derived from the peak of the frequency spectrum of the transformed signal.

Frequency-domain (FD) PTA methodologies can offer alternative detection and imaging schemes with concrete advantages over pulsed laser photoacoustics. These advantages include: (a) Low fluence of the harmonic or frequency-swept (chirped) laser modulation, with the concomitant advantage of a much higher tissue damage threshold. A combination of harmonically modulated and chirped detection methodologies[12] can overcome the possible disadvantage of lower signal levels under single-frequency harmonic modulation at high, thermally adiabatic frequencies ($\sim$ MHz), while retaining the speed and wide temporal range of pulsed laser responses. The superior signal-to-noise ratio of the ultranarrow lock-in amplifier bandpass filter can offset much of the SNR deterioration at MHz frequencies. Frequency chirps may also recover the strength of the high-frequency Fourier components through fast-Fourier transformation of the frequency-domain transfer function to time-domain impulse-response, thus matching the major advantage of pulsed-laser excitation; (b) Depth profilometry over a very wide range of frequencies. The depth range in turbid media depends on the acoustic velocity and the optical extinction coefficient at the probe wavelength. Therefore, through precise time gating by use of optimal boundary (minimum and maximum) frequencies in a laser chirp, depth localization can be effected in a much more controllable fashion than with a pulsed laser. The chirp can be further tailored to center around a particular feature of interest, thus offering a high degree of depth controllability and efficient rejection of undesirable acoustic reflections outside the time gate, thus minimizing unwanted interference effects. (c) Possible parallel multichannel lock-in signal processing and image generation in quasireal time;[14,15] (d) A substantially wider signal dynamic range through use of lock-in filtering; and (e) A simple instrumental normalization procedure through division with a reference signal in the frequency-domain, as opposed to nontrivial deconvolution in the time domain, especially with highly nonlinear (e.g., resonant) ultrasonic transducers. Yet, FD and/or hybrid methods have not been pursued historically in biomedical PTA imaging.

In this paper we report the theoretical and experimental development of a new frequency-swept lock-in PTA depth profilometric imaging methodology for ultimate use with biomedical turbid media. The problem of linear PTA pressure wave generation from a solid immersed in a liquid is addressed and a mathematical model for a three-layered liquid–solid–liquid system is formulated. A modulated cw laser beam incident on the top surface of an absorbing solid is considered as the source of PTA waves inside the solid. Coupled small-amplitude (linear) wave equations are solved in the solid and fluid, and the resulting predictions are compared to experimental data obtained using a laser operating within the relatively nonabsorbing range of human tissue (1064 nm) and a commercial acoustic transducer as the receiver. The present one-dimensional model also accounts for acoustic attenuation and optical absorption effects. The single-frequency model was further extended to include linearly frequency-swept laser amplitude modulation via chirping the laser source, and theoretical data were compared to experimental results on a rubber sample immersed in water. The results indicate that the frequency-domain PTA field is closely associated with the location and dimensions of a subsurface object, its acoustic impedance, acoustic damping property, and optical absorption coefficient. By scanning across a sample surface area of interest, 2D and/or 3D images can be obtained by combining the depth profilometric scans obtained at each point and at a fixed acoustic delay time. Preliminary experimental results using artificial subsurface defects in rubber and solid tissue phantoms are also presented. This method allows one to increase subsurface feature resolution by time gating and imaging only selected depth slices to the exclusion of other overlying or underlying features.

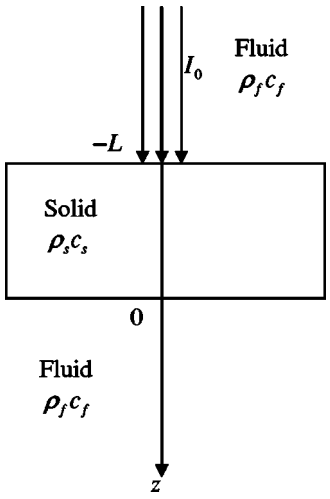

FIG. 1. Geometry used for formulating the frequency-swept lock-in PTA problem.

II. THEORY OF PHOTO-THERMO-ACOUSTIC WAVE GENERATION IN LAYERED STRUCTURES

A. Coupled PTA boundary value problems

Figure 1 shows the geometry used for the one-dimensional mathematical model. The configuration closely corresponds to the experimental geometry. It contains three coupled layers: the top and bottom layers are composed of a fluid, with the middle layer composed of a solid. The top layer is assumed to be semi-infinite fluid and occupies the spatial region $-\infty < z \leqslant -L$. It has density ρ_f, and speed of sound c_f. The solid layer has thickness L, density ρ_s, speed of sound c_s, specific heat at constant pressure C_{Ps}, optical absorption coefficient at the laser wavelength μ_a, bulk modulus K_s, and isobaric volume expansion coefficient β_s. For the quantitative measurements on nonturbid media presented in this work, the scattering coefficient of the medium and the contributions and complications of the diffuse photon-density wave replacing the purely absorbing ther-

moacoustic signal source are ignored for simplicity. However, the mathematical formalism to deal with these issues has been developed[16,17] and will be applied to quantitative measurements of light-scattering phantoms, such as those used qualitatively in Sec. III, in a future publication. Since the thermal diffusion length, $\mu(\omega)=\sqrt{2\alpha_s/\omega}$, is negligible compared to the diameter of the heat source ($\sim$3 mm), the mathematical model can be considered in the 1D regime. The bottom layer extends from $0\leqslant z<\infty$. We do not consider the finite thickness of the bottom layer because in our experiments no reflections from the fluid–container interface were observed.

An analytical solution of the coupled PTA problem in the form of spectral integrals can be obtained by converting the time-domain equations to their frequency-domain counterparts using Fourier transforms (FTs).[18,19] The spectral Fourier component of the heat conduction equation in the solid is the thermal-wave equation

$$\frac{\partial^2}{\partial z^2}\theta_s(z,\omega)-\left(\frac{i\omega}{\alpha_s}\right)\theta_s(z,\omega)=-\frac{1}{\lambda_s}H(z,\omega),\quad -L\leqslant z\leqslant 0, \tag{1}$$

where $\theta_s(z,\omega)$ is the temperature rise above ambient. α_s and λ_s are, respectively, the thermal diffusivity and conductivity of the solid medium. The spectral component $H(z,\omega)$ at any angular frequency ω of the thermal source is given by

$$H(z,\omega)=\mu_a I_0 e^{-\mu_a(L+z)+i\omega t}. \tag{2}$$

Here, I_0 is the laser fluence and $e^{i\omega t}$ is the modulation factor. The term $e^{i\omega t}$ is implied in each term of the solutions and will be omitted hereafter. Since the thermal diffusion length, $\mu(\omega)=\sqrt{2\alpha_s/\omega}$, is negligible compared to the sample thickness, the solid layer can be considered as semi-infinite. The general solution of Eq. (1) is

$$\theta_s(z,\omega)=Ge^{-\sigma_s(z+L)}+Ee^{-\mu_a(z+L)}, \tag{3}$$

where $\sigma_s^2=i\omega/\alpha_s$ is the complex thermal-wave diffusion coefficient in the solid. G is an unknown coefficient that needs to be determined and E is the source term defined as

$$E=\frac{\mu_a I_0}{\lambda_s(\sigma_s^2-\mu_a^2)}. \tag{4}$$

Assuming a nonviscous fluid with no direct internal PTA source, the FT component of the heat conduction equation inside such a fluid can be written as

$$\frac{\partial^2}{\partial z^2}\theta_f(z,\omega)-\left(\frac{i\omega}{\alpha_f}\right)\theta_f(z,\omega)=0,\quad -\infty<z\leqslant -L,$$
$$0\leqslant z<\infty, \tag{5}$$

where $\theta_f(z,\omega)$ is the temperature rise and α_f is the thermal diffusivity of the fluid. The general solution for Eq. (5) can be written as

$$\theta_f(z,\omega)=Fe^{\sigma_f(z+L)}. \tag{6}$$

Here, F is an unknown coefficient and $\sigma_f^2=i\omega/\alpha_f$.

By using the thermal boundary conditions at the fluid/solid interface

$$\theta_f(-L,\omega)=\theta_s(-L,\omega),$$

$$\lambda_s\frac{\partial}{\partial z}\theta_s=\lambda_f\frac{\partial}{\partial z}\theta_f, \tag{7}$$

one can determine the constants F and G as

$$F=\frac{E(\lambda_s\sigma_s-\lambda_s\mu_a)}{(\lambda_f\sigma_f+\lambda_s\sigma_s)}, \tag{8}$$

$$G=-Eb_{sf}, \tag{9}$$

where

$$b_{sf}=\frac{(\lambda_s\mu_a+\lambda_f\sigma_f)}{(\lambda_f\sigma_f+\lambda_s\sigma_s)} \tag{10}$$

By introducing in the solid a particle/molecule displacement potential, $\phi_s(z,\omega)$, the coupled wave equations in the solid and fluid can be easily solved. The displacement potential is related to the displacement vector, $U_s(z,\omega)$, as

$$U_s(z,\omega)=\frac{\partial}{\partial z}\phi_s(z,\omega),\quad -L\leqslant z\leqslant 0. \tag{11}$$

Due to laser PTA excitation by a large spot-size laser beam, only longitudinal waves are assumed to propagate in an isotropic solid. This assumption allows the use of the Helmholtz equation, which is satisfied by the displacement potential, ϕ_s

$$\frac{\partial^2}{\partial z^2}\phi_s(z,\omega)+k_s^2\phi_s(z,\omega)=\left(\frac{K_s\beta_s}{\rho_s c_s^2}\right)\theta_s(z,\omega), \tag{12}$$

where $k_s=\omega/c_s$ is the acoustic wave number in the solid for small-amplitude acoustic perturbations. The general solution to this equation is

$$\phi_s(z,\omega)=Ae^{ik_s z}+Be^{-ik_s z}+Ce^{-\sigma_s(z+L)}+De^{-\mu_a(z+L)}. \tag{13}$$

Here, A and B are integration constants to be determined. Constants C and D are found to be

$$C=\frac{-\mu_a I_0 K_s\beta_s b_{sf}}{\rho_s c_s^2\lambda_s(\sigma_s^2-\mu_a^2)(\sigma_s^2+k_s^2)},$$

$$D=\frac{\mu_a I_0 K_s\beta_s}{\rho_s c_s^2\lambda_s(\sigma_s^2-\mu_a^2)(\alpha^2+k_s^2)}. \tag{14}$$

Inside the fluid, since wave sources have a potential nature, liquid motion will be potential motion. By introducing a scalar potential of the velocity field

$$v(z,\omega)=\frac{\partial}{\partial z}\psi_{fi}(z,\omega),\quad -\infty<z\leqslant -L,\quad 0\leqslant z<\infty, \tag{15}$$

where the subscript $i=1,2$ indicates the top and bottom fluid, respectively, one can obtain the photo-thermo-acoustic wave equation [Eq. (16)] for a nonviscous fluid[19]

$$\frac{\partial^2}{\partial z^2}\psi_{fi}(z,\omega)+k_f^2\psi_{fi}(z,\omega)=0, \tag{16}$$

where $k_f=\omega/c_f$ is the wave number for small-amplitude acoustic perturbations in the fluid.

The small-amplitude pressure change in the fluid is related to the velocity potential, Ψ_{fi}, by

$$P(z,\omega) = -i\omega\rho_f \psi_{fi}(z,\omega). \tag{17}$$

The general solutions to Eq. (16) can be written as

$$\psi_{f1}(z,\omega) = C_1 e^{ik_f(z+L)}, \quad -\infty < z \leqslant -L,$$

$$\psi_{f2}(z,\omega) = C_2 e^{-ik_f z}, \quad 0 \leqslant z < \infty. \tag{18}$$

The constants (A,B,C_1,C_2) in Eqs. (13) and (18) can be determined through the boundary conditions of stress and velocity continuity at the two interfaces $z=0,-L$[19]

$$\rho_s c_s^2 \frac{\partial^2}{\partial z^2}\phi(0,\omega) - K_s\beta_s\theta_s(0,\omega) = -P(0,\omega) = i\omega\rho_f\psi_{f2}(0,\omega),$$

$$\rho_s c_s^2 \frac{\partial^2}{\partial z^2}\phi(-L,\omega) - K_s\beta_s\theta_s(-L,\omega) = P(-L,\omega) = i\omega\rho_f\psi_{f1}(-L,\omega),$$

$$i\omega\frac{\partial}{\partial z}\phi_s(0,\omega) = \frac{\partial}{\partial z}\psi_{f2}(0,\omega),$$

$$i\omega\frac{\partial}{\partial z}\phi_s(-L,\omega) = \frac{\partial}{\partial z}\psi_{f1}(-L,\omega). \tag{19}$$

Using the boundary conditions (19), coefficient C_1 can be determined as

$$C_1(\omega) = \frac{\mu_a I_0 K_s\beta_s c_f [A_n(\omega)e^{ik_s L} + B_n(\omega)e^{-ik_s L} + 2i\omega c_f b_{sf}(\mu_a^2+k_s^2)(i\sigma_s\rho_f + k_f\rho_s)e^{-\sigma_s L} + C_n(\omega)]}{c_s\omega\lambda_s(\sigma_s^2-\mu_a^2)(\mu_a^2+k_s^2)(\sigma_s^2+k_s^2)[(\rho_s c_s+\rho_f c_f)^2 e^{ik_s L} - (\rho_s c_s - \rho_f c_f)^2 e^{-ik_s L}]},$$

where

$$A_n(\omega) = (\rho_s c_s + \rho_f c_f)[ic_s k_s^2(\sigma_s^2 + k_s^2 - \mu_a^2 b_{sf} - k_s^2 b_{sf}) - \omega(\mu_a\sigma_s^2 + \mu_a k_s^2 - \sigma_s\mu_a^2 b_{sf} - \sigma_s k_s^2 b_{sf})],$$

$$B_n(\omega) = (\rho_s c_s - \rho_f c_f)[\omega(\mu_a\sigma_s^2 + \mu_a k_s^2 - \sigma_s\mu_a^2 b_{sf} - \sigma_s k_s^2 b_{sf}) + ic_s k_s^2(\sigma_s^2 + k_s^2 - \mu_a^2 b_{sf} - k_s^2 b_{sf})],$$

and

$$C_n(\omega) = 2i\omega c_f(\sigma_s^2 + k_s^2)(-k_f\rho_s - i\mu_a\rho_f)e^{-\mu_a L}. \tag{20}$$

Finally, the spectral component of the experimentally measurable pressure wave in the front fluid can be written as

$$P(z,\omega) = -i\omega\rho_f C_1(\omega)e^{ik_f(z+L)}. \tag{21}$$

B. Acoustic attenuation effects

Equation (12) for the FT of the one-dimensional displacement potential can be modified to allow for acoustic attenuation effects in the solid. The resulting Helmholtz equation can be written as

$$\frac{\partial^2}{\partial z^2}\phi_s(z,\omega) + k_{\gamma s}^2\phi_s(z,\omega) = \left(\frac{K_s\beta_s}{\rho_s c_s^2}\right)\theta_s(z,\omega),$$

where

$$k_{\gamma s} = \frac{\omega}{c_s} - i\frac{\gamma\omega}{2\pi}. \tag{22}$$

Here, γ is the acoustic attenuation coefficient with dimensions of Nepers/m. By assuming the wave number, $k_{\gamma s}$, to be complex, its imaginary part would account for the acoustic absorptive properties of the material. Therefore, the effects of acoustic attenuation can be incorporated in the PTA pressure wave equations by simply substituting $k_{\gamma s}$ for k_s in all relevant spectral equations described above.

C. Special case: Optically opaque solid

For an optically opaque solid, the exponential term, $e^{-\mu_a L}$, can be ignored due to the vanishingly small optical absorption length, μ_a^{-1}. Therefore, by using the boundary conditions [Eq. (19)], coefficient C_1 can be relatively simplified

$$C_1(\omega) = \frac{\mu_a I_0 K_s\beta_s c_f [A_n(\omega)e^{ik_s L} + B_n(\omega)e^{-ik_s L} + 2i\omega c_f b_{sf}(\mu_a^2+k_s^2)(i\sigma_s\rho_f + k_f\rho_s)e^{-\sigma_s L}]}{c_s\omega\lambda_s(\sigma_s^2-\mu_a^2)(\mu_a^2+k_s^2)(\sigma_s^2+k_s^2)[(\rho_s c_s+\rho_f c_f)^2 e^{ik_s L} - (\rho_s c_s - \rho_f c_f)^2 e^{-ik_s L}]},$$

where

$$A_n(\omega) = (\rho_s c_s + \rho_f c_f)[ic_s k_s^2(\sigma_s^2 + k_s^2 - \mu_a^2 b_{sf} - k_s^2 b_{sf}) - \omega(\mu_a\sigma_s^2 + \mu_a k_s^2 - \sigma_s\mu_a^2 b_{sf} - \sigma_s k_s^2 b_{sf})],$$

$$B_n(\omega) = (\rho_s c_s - \rho_f c_f)[\omega(\mu_a\sigma_s^2 + \mu_a k_s^2 - \sigma_s\mu_a^2 b_{sf} - \sigma_s k_s^2 b_{sf}) + ic_s k_s^2(\sigma_s^2 + k_s^2 - \mu_a^2 b_{sf} - k_s^2 b_{sf})]. \tag{23}$$

Again, by substituting coefficient, $C_1(\omega)$, into Eq. (21), one can obtain the spectral component of the pressure wave in the top fluid layer, which is a complex number. Both the amplitude and phase of the pressure field will be plotted and compared to the experimental frequency-scan results in Sec. III.

The frequency-domain numerical results will be further converted into time domain using inverse Fourier transfor-

TABLE I. Optical and elastic properties used as input parameters for the mathematical model.

μ_s (1/cm)	K_s (N/m^2)	β_s (1/C)	c_s (m/s)	c_f (m/s)	ρ_s (kg/m^3)
100	1.5×10^9	6×10^{-4}	1600	1474	1320
ρ_f (kg/m^3)	λ_s (W/mK)	λ_f (W/mK)	α_s (m^2/s)	α_f (m^2/s)	γ (Nepers/m)
998	0.13	0.61	0.06×10^{-6}	0.1×10^{-6}	55×10^{-6}

mation (IFT) and used as theoretical fits to the experimental data in frequency-swept measurements (Sec. IV).

III. PTA FREQUENCY-SCAN SIMULATIONS, INSTRUMENTATION, AND EXPERIMENTAL RESULTS

Theoretical simulations were performed for the simple case of a black rubber sample immersed in water. There are two reasons to use rubber samples in this project. First is to verify the mathematical model. The numerically simulated results show the difference between PTA signals generated by an opaque and a translucent layer. The rubber sample is an example of such an opaque solid. Second, the rubber samples can provide us with preliminary results to test and optimize the instrumental aspects of the imaging system while we are still trying to achieve a better understanding of wave generation from scattering phantoms. Two input parameters, the thickness of the solid and its optical absorption coefficient, were changed independently for each simulation to illustrate the frequency-domain PTA signal generation through the developed theory. Table I (Refs. 20–22) presents the optical and elastic properties used as input parameters for the mathematical model. For a fully opaque solid, Eqs. (23) and (21) were used to calculate the laser-induced acoustic field within the actual experimental frequency range. Figures 2(a) and (b) display the theoretical amplitude and phase of the pressure field obtained from a 2.5-mm-thick rubber piece. Figures 3(a) and (b) are the numerically simulated results obtained from 5-mm-thick rubber using the developed theory. The frequency-domain amplitude plots contain a series of oscillations, superposed on a decaying envelope. Due to the intermediate step of optical energy conversion into thermal waves, the spectral energy content decreases with increasing laser modulation frequency. This well-known thermal-wave effect controls the further conversion of thermal energy into acoustic waves, thus turning the PTA signal envelope into a low-pass-equivalent filter. The amplitude oscillations are due to standing acoustic waves between the top and bottom surfaces of the rubber. For an opaque solid, laser light is only absorbed at the top surface of the solid, where thermoelastic waves are then generated. In the one-dimensional model, the acoustic waves propagate in two directions, upward into the fluid and downward into the solid material. In a 3D model, this longitudinal character of the photo-thermo-acoustic wave would still prevail as the signal is dominated by boundary reflections. The wave components reflected from the bottom surface will lag in phase compared to those generated at the top surface of the solid. Under harmonic excitation, a standing wave will be formed, so that at frequencies

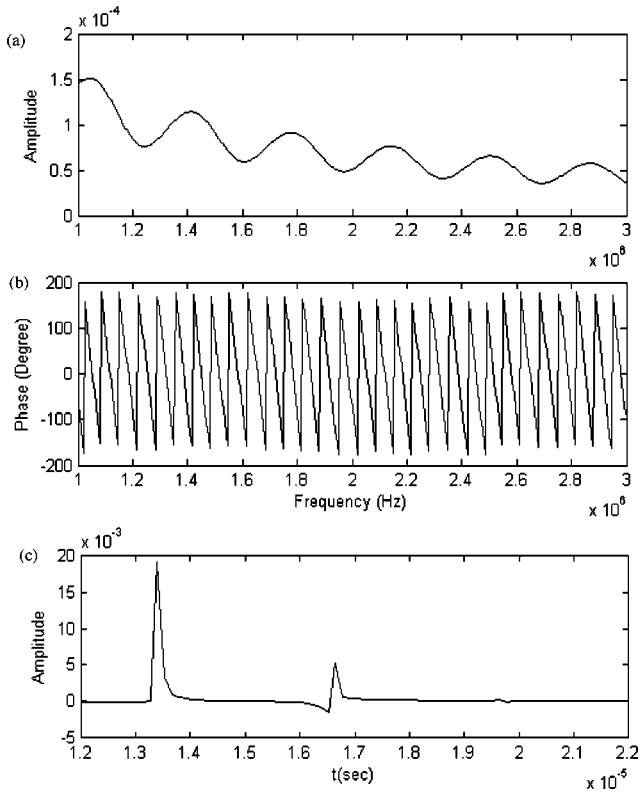

FIG. 2. Frequency-domain (amplitude and phase) and time-domain (amplitude) simulation of the PTA pressure field obtained using a 2.5-mm-thick rubber piece ($\mu_a = 100\ cm^{-1}$).

$$f_n = \frac{(2n+1)c_s}{4L}, \quad n = 0,1,2,3..., \tag{24}$$

and

$$f_n' = \frac{nc_s}{2L}, \quad n = 1,2,3..., \tag{25}$$

there will be destructive interference minima and constructive interference maxima, respectively, as shown in the amplitude plots of Figs. 2(a) and 3(a). It is clear that the frequency values, f_n and f_n' are related to the thickness of the opaque solid.

The PTA phase patterns of Figs. 2(b) and 3(b) are related to sample thickness, the acoustic impedance at the sample–water interface, and the location of the receiver. Despite the appearance of these curves, the phase of the pressure field is continuous as a function of frequency. Since phase is measured within the range of $\pm\pi$, a 360-deg discontinuity occurs as the value of phase reaches $+\pi$ or $-\pi$, both experimentally and computationally.

Figures 2(c) and 3(c) are the time-domain amplitude plots of the simulated pressure field, corresponding to Figs. 2(a) and 3(a), respectively. These time-domain plots were converted from their frequency-domain counterparts using the inverse Fourier transformation (IFT). The two peaks in each plot indicate the acoustic waves generated at the top surface and reflected from the bottom surface of the solid. The delay time between the two peaks is equal to twice the thickness of the solid, divided by the speed of sound in the medium.

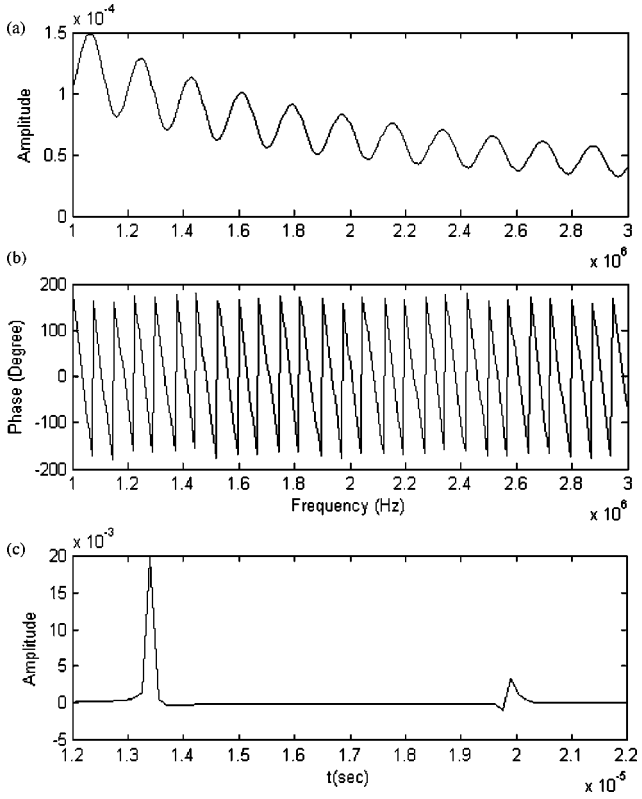

FIG. 3. Frequency-domain (amplitude and phase) and time-domain (amplitude) simulation of the PTA pressure field obtained using a 5-mm-thick rubber piece ($\mu_a = 100\ \mathrm{cm}^{-1}$).

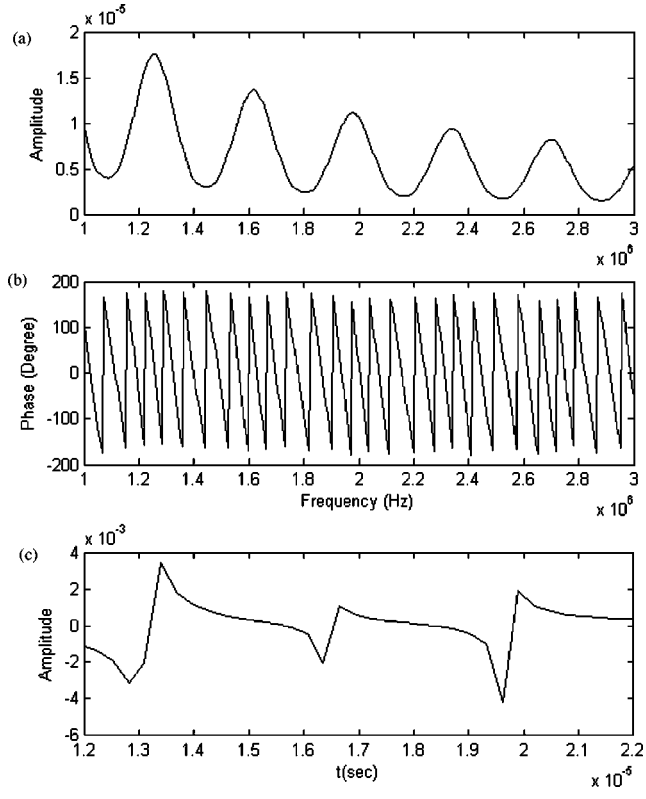

FIG. 4. Frequency-domain (amplitude and phase) and time-domain (amplitude) simulation of the PTA pressure field obtained from a 5-mm-thick translucent solid with the same thickness of rubber in Fig. 3 and optical absorption coefficient $\mu_a = 4\ \mathrm{cm}^{-1}$.

To illustrate the effects of varying optical absorption (penetration) depth on the PTA signal, Fig. 4 features the same rubber material as Fig. 3, but with a smaller optical absorption coefficient, representing a translucent solid. For such a solid, laser light can penetrate deeper into the bulk and create a distributed light/heat source. Due to the distributed heat sources, thermoelastic waves are generated by local compressions and expansions. All these acoustic waves created throughout the thickness of the translucent solid contribute to the total pressure field. Although the thicknesses of the solids in Figs. 3 and 4 are the same, different interference patterns are observed due to the differences in absorption depth. As for the phase plots, no significant changes can be observed between Figs. 3(b) and 4(b), owing to the very large range of phases involved. Figure 4(c) is the IFT time-domain amplitude plot corresponding to Fig. 4(a), and it contains three major peaks. The first two peaks are caused by the acoustic waves generated at the top and bottom liquid–solid interfaces. The third peak is caused by the first reflection of acoustic waves from the bottom surface. Comparing Fig. 4(c) to Fig. 3(c), which is obtained from an opaque solid with the same thickness and similar thermoelastic properties, the delay time between the first two peaks in Fig. 4(c) is half of that in Fig. 3(c). This is so because the acoustic waves created by the subsurface-distributed light/heat sources at the back interface of the translucent solid propagate backwards and are detected without requiring the forward wave to undergo reflections from the bottom surface. Another important feature caused by the decrease of the optical absorption coefficient is the decrease in signal amplitude and broadening of PTA response, which is also shown in Fig. 4(c). This feature is caused by the deeper penetration of light and a more even distribution of heat source inside the material.

A block diagram of the experimental setup for the frequency scan measurements is shown in Fig. 5. The optical source used to generate PTA pressure waves was an ytterbium fiber laser (IPG Photonics, 1064 nm). Using a function generator (Stanford Research Systems, DS345) to drive the acousto-optic modulator (Neos Technologies, N15180-1.06-Gap) chosen for its optimal modulation depth, the intensity of the laser beam was modulated harmonically at selected frequencies. The laser beam was focused onto the specimen. An acoustic mirror (Panametrics, F102) with a small hole to allow passage of the incident light beam was used to reflect

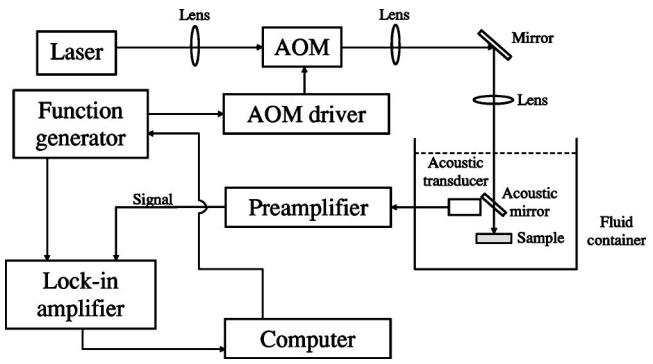

FIG. 5. Block diagram of the experimental PTA setup used for frequency scans.

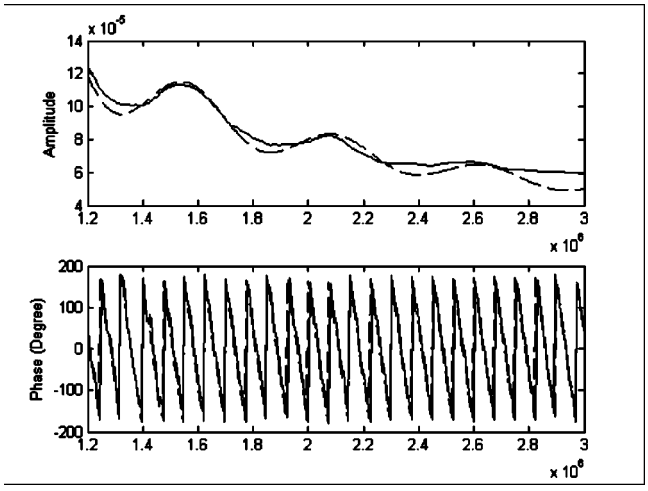

FIG. 6. Frequency-domain amplitude and phase of the PTA pressure field obtained from a 1.8-mm-thick rubber piece. Solid line: experimental results. Dashed line: best-fitted numerical results.

the sound waves to a commercial acoustic transducer (Panametrics, V382). The received signal was amplified by a preamplifier (Panametrics, 5676) and sent to a high-frequency lock-in amplifier (Stanford Research Systems, SR844). A computer program (MATLAB 6.0) was used to control the frequency of the function generator and acquire the data from the lock-in amplifier.

The specimen used for the frequency scan measurements was a 1.8-mm-thick piece of rubber immersed in water. Frequency scans were performed at several lateral positions. At each position, the scan was repeated five times within the frequency range of 1.2–3 MHz. The frequency step size was 50 kHz. The results at each lateral position were coadded and averaged to eliminate white noise. The frequency spectra were normalized using the transfer function curve of the acoustic transducer supplied by the manufacturer.

The experimental and best-fitted frequency-scan results using the system of Fig. 5 and Eq. (23) for an opaque solid are shown in Fig. 6. The thickness and density of the rubber sample were measured to be 1.8 mm and 1320 kg/m^3, respectively. The measured room temperature was 24 °C, from which the density and the speed of sound in water were calculated[23] to be 998 kg/m^3 and 1489 m/s, respectively. To obtain the best fits to the entire frequency record of the pressure responses, the exact values of the bulk modulus, K_s, isobaric volume expansion coefficient, β_s, acoustic attenuation coefficient, γ, thermal diffusivities, $\alpha_{f,s}$, and thermal conductivities, $\lambda_{f,s}$, were not as important as the speed of sound, and the optical absorption coefficient of the rubber sample. For these secondary parameters, the listed values in Table I were used for the numerical simulations. The important parameters used for the theoretical fits were the speed of sound, $c_s = 1800$ m/s, and the optical absorption coefficient, $\mu_a = 100$ cm^{-1}. The value of the optical absorption coefficient is close to the upper limit of the resolvable absorption coefficient range. Although this number is not excessively high, it is well-known that PA saturation sets in at around 5×10^3 cm^{-1}.[24] Above this limit, no significant changes were observed for the amplitude and phase plots, and the solid is considered as a black absorber. A good agreement is observed in Fig. 6, between the measured and calculated pressure field against frequency. The slight discrepancy in the amplitude plot is within the estimated range of uncertainties of the measurement system, which was mainly caused by nonuniformity of the specimen and system noise of the electrical circuit.

IV. PTA FREQUENCY SWEEPS AND HETERODYNED SUBSURFACE IMAGING

A rapid frequency-scanning (chirp generation) system was designed and implemented to allow for fast PTA depth profilometry of subsurface inhomogeneities through a wide range of depths at a fixed spatial coordinate. Besides their advantage of speed for full frequency-spectrum acquisition compared to point-to-point frequency scans, another major feature of frequency-swept thermoacoustic signals is their ability to be Fourier transformed into a time-delay domain inverse spectrum which carries the depth profilometric information in a series of time sequences equivalent to the impulse response of the acoustic system.[25,26] Therefore, frequency-swept PTA signals are hybrid between time- and frequency domains,[12] a unique property which can be used to enhance signal-to-noise ratio significantly through heterodyning and lock-in noise filtering. The block diagram of the frequency-sweep heterodyne subsystem used to modify the PTA signal generation and detection part of Fig. 5 is shown in Fig. 7. A linear frequency sweep (chirp) signal was generated by a function generator (FG1) to modulate the intensity of the ytterbium laser. The chirp signal of FG1 was triggered by a delay-pulse generator (Stanford Research Systems, DG 535), which was also used to trigger the second function generator (FG2). The output of FG2 was mixed with the output of the PTA ultrasonic transducer using a mixer (Mini-circuits, ZAD-3). The output of the mixer was further sent to a low-pass filter (LPF1, Stanford Research Systems, SR 640). This signal was then mixed with a single harmonic frequency, ω_0 using a second mixer. The single-frequency signal was generated by the internal oscillator of the high-frequency lock-in amplifier (LIA; Stanford Research Systems SR 844). The output signal of mixer 2 was filtered using the second low-pass filter (LPF2) and then sent to the LIA as the input signal. The amplitude and phase of the LIA output were stored in a computer for display and analysis.

The PTA signal generation flow chart associated with the circuit of Fig. 7 is described in Fig. 8. The chirp signal generated by FG1 can be written as $\cos[(a+bt)t]$, where $a = 1$ MHz is the starting frequency and $b = 4$ MHz/ms is the sweep rate. This chirp signal was triggered by the DG 535 delay-pulse generator, which also triggered FG2. The output of FG2, delayed by a controlled time, τ, through the delay pulse generator can be written as $\cos\{[a+b(t-\tau)]t\}$. The intensity of the laser beam was modulated by the acousto-optic modulator according to the chirp signal generated by FG1. At the acoustic transducer, the received signal can be written as $\cos\{[a+b(t-(z/c))]t\}$, where z represents the depth at which the acoustic signal originates, and c is the speed of sound in the probed medium. Due to the linear relationship between the depth and the delay time when the transducer

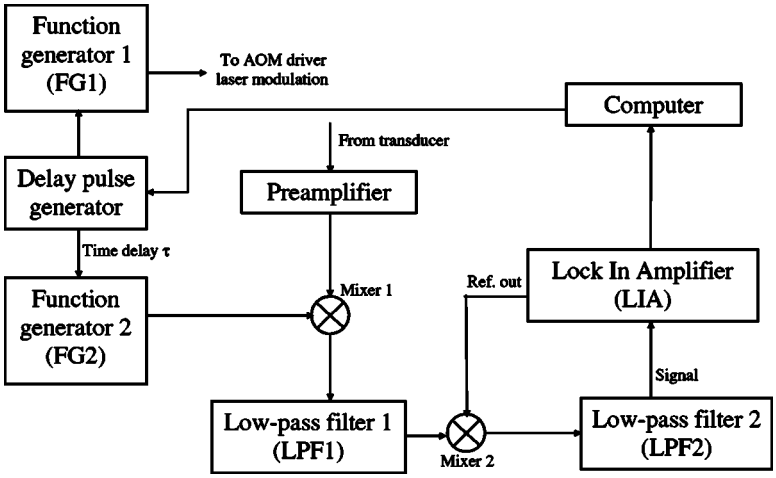

FIG. 7. Block diagram of the circuit used in the PTA system of Fig. 5 for frequency-swept (chirp) heterodyned depth profilometric scanning imaging.

receives the signal, this expression shows that the information at a certain depth can be related with the frequency components of the chirp signal. At mixer 1, the frequency components from the two input channels underwent addition and subtraction. The resulting high-frequency part was then removed by low-pass filter 1. The remaining low-frequency part of the signal was downshifted and contained a wide spectrum of frequencies, each with time-delayed information. Since both the input signals of mixer 1 contained the same starting frequency, a, this component was canceled out after subtraction. The output signal from LPF1 can be written as $\cos\{[b(\tau-(z/c))]t\}$. To perform PTA depth profilometry, mixing this output (second mixer) with a single harmonic fixed frequency, ω_0, generated by the internal oscillator of the LIA, and low-pass filtering the two sidebands of the mixed signal, yielded an output which can be represented by $\cos\{[\omega_0-b(\tau-(z/c))]t\}$. The frequency downshifted output was detected by the LIA. By scanning the chirp delay time, τ, a nonzero LIA signal output was expected at ω_0 only when $\tau=z/c$. Therefore, τ scans at a fixed spatial coordinate are equivalent to depth coordinate scans and can yield information from different probe depths in the sample at a fixed lateral coordinate point. Scanning over a predetermined two-dimensional area of the sample will generate a subsurface 3D image.

The solid line in Fig. 9 is the result of a single (x,y) point scan using the PTA imaging system, while the dashed line is the simulated result. The chirp signal covered a frequency range from 1 to 5 MHz and the step size of the delay time used for the scan was 0.1 μs. The specimen was a 5.4-mm-thick rubber piece, which had the same material properties as the one used for frequency-scan tests. The frequency-domain simulated result was calculated by substituting the thickness, material properties, and the chirp frequency range into Eqs. (23) and (21). The corresponding time-domain pressure field was obtained by applying inverse Fourier transformation to the frequency-domain result. The peaks were generated by solid–liquid interface reflections of acoustic waves. Good agreement was obtained between the numerical and experimental results. Even though the laser beam was focused, thus creating in principle a 3D PTA pro-

FG1: $\cos((a+bt)t)$;

a – starting freq.; b – sweep rate

Acoustic transducer: $\cos[(a+b(t-\frac{z}{c}))t]$

FG2: $\cos[(a+b(t-\tau))t]$

Mixer1+LPF1: $\cos[b(\tau-\frac{z}{c})t]$

LIA's internal oscillator: $\cos[\omega_0 t]$

Mixer2+LPF2: $\cos[(\omega_0-b(\tau-\frac{z}{c}))t]$

LIA registers a signal only when : $\tau = \frac{z}{c}$

FG —— Function generator
LPF —— Low pass filter
LIA —— Lock-in amplifier

FIG. 8. Frequency-swept and heterodyned PTA signal generation flow chart.

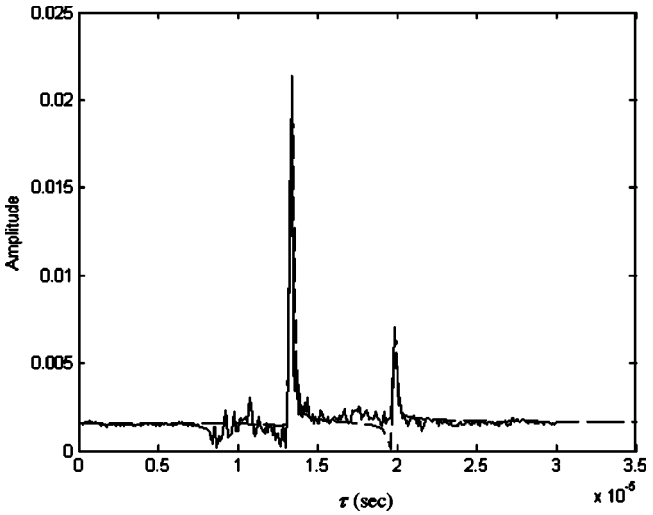

FIG. 9. A single-point scan of a 5.4-mm-thick rubber piece using the PTA chirp heterodyne scanning system. Solid line: experimental data; dashed line: numerical fits to the theory. The horizontal axis indicates time delay $\tau=z/c$.

file, the reflection spectrum from a short distance between interfaces is expected to be very similar to the 1D situation and to be adequately interpreted by our 1D theory, as observed. An interesting feature here is the increase of ''background'' noise in the measured pressure field after 8 μs. Eight μs corresponds to the delay time required by the acoustic transducer to receive the first echo generated at the acoustic mirror, Fig. 5. The background noise is due to the multiple reflections of sound waves within the probed medium.

Although both the single-frequency scan system (Fig. 5) and the chirp scan system (Fig. 7) can perform depth profilometric measurements, the PTA chirp scan system has significant advantages of precise depth control, fast scanning speed, and high signal-to-noise ratio. The modified chirp scan system shown in Fig. 7 performs an inverse Fourier transformation to convert the frequency-domain measured pressure field into time-domain signals, which carry the depth profilometric information in a series of time sequences equivalent to the impulse response of an acoustic system. This important step makes it possible to construct an operator-controlled subsurface slice-by-slice image in 3D space. In order to obtain a frequency-scan plot, as shown in Fig. 6, one has to perform point-by-point frequency-scans using the single frequency scan system, followed by signal averaging and normalization, which significantly hampers the operating speed. On the other hand, the chirp scan system has the capability to perform full frequency-spectrum acquisition in $<$ms duration. In conclusion, through heterodyning and lock-in noise filtering, the PTA chirp scan system can generate time-domain equivalent signals with a high signal-to-noise ratio, using a fraction of operating time.

Figure 10 presents the depth profilometric amplitude and phase images of a 2D scan over another rubber sample, which had a curved top surface. The meaning of a 2D scan is actually a surface line scan containing a full depth scan at each surface coordinate point. The thickness of this sample was 7 mm at the center and 3 mm around the edges. The scan was performed from left to right with a spatial step size of around 1 mm. The step size of the delay time was 0.1 μs, which corresponds to a distance of around 150 μm in water. The images clearly show the top surface and the bottom surface at two edges of the solid. However, at the center part of the cross section, the bottom surface is not visible, due to excessive acoustic attenuation in the thicker body of the material. From this result it was determined that the detectable thickness of this opaque rubber sample was around 3 mm.

Preliminary depth profilometric scans using solid phantoms with optical and acoustical properties resembling those of blood-deficient (normal) and blood-rich (vascularized) tissue were also performed. The solid phantoms are homogeneous, 3-mm-thick, monolithic, and made of polyacrylamide with different absorption coefficients. The reason we show this set of results is to partially verify the validity of the theory and compare the PTA signals obtained from an opaque vs a translucent solid without scattering. The second reason we present these results is to show potential applications of this technique to subsurface tissue imaging. The optical absorption coefficients at 1064 nm wavelength are

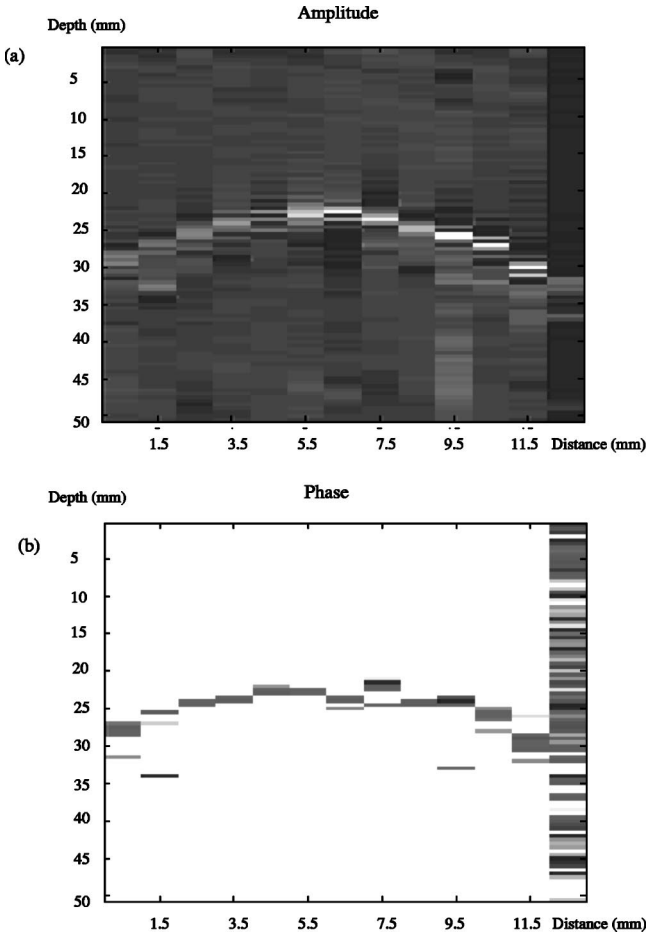

FIG. 10. Depth profilometric images of a rubber sample with curved top surface obtained using the PTA chirp heterodyne scanning system. (a) Amplitude (b) Phase.

around 0.1 and 10 cm^{-1} for blood-deficient dermis and oxygenated blood, respectively.[27] The effective scattering coefficient for breast tissue is around 1.2 cm^{-1}.[6] To illustrate the effects of varying optical absorption coefficient (optical penetration depth) on the PTA signal, depth profilometric scans were performed on a set of single-layered solid phantoms made of polyacrylamide, diluted with different percentages of India ink to closely mimic the absorption and scattering properties of human tissue. The thickness of the solid phantoms was 3 mm. Their optical absorption coefficients, μ_a, and effective optical scattering coefficients, μ_s', ranged from 3 to 15 cm^{-1} and 0.15 to 3 cm^{-1}, respectively. These optical properties were obtained from the literature.[28]

Figure 11 shows three sets of 1D scan results (amplitude and phase) obtained from samples with different μ_a and μ_s'. A direct quantitative comparison between the experimental and numerical results is not practical, since our model does not include the scattering effects of the solid. Following the developed formalism,[16,17] these issues will be addressed in forthcoming publications. However, certain features observed from the experimental results still agree with the predictions of the present mathematical model. (A) A decrease in optical absorption coefficient always results in diminished signal amplitude and broadening of the PTA response. (B) The peaks and troughs corresponding to the top and bottom

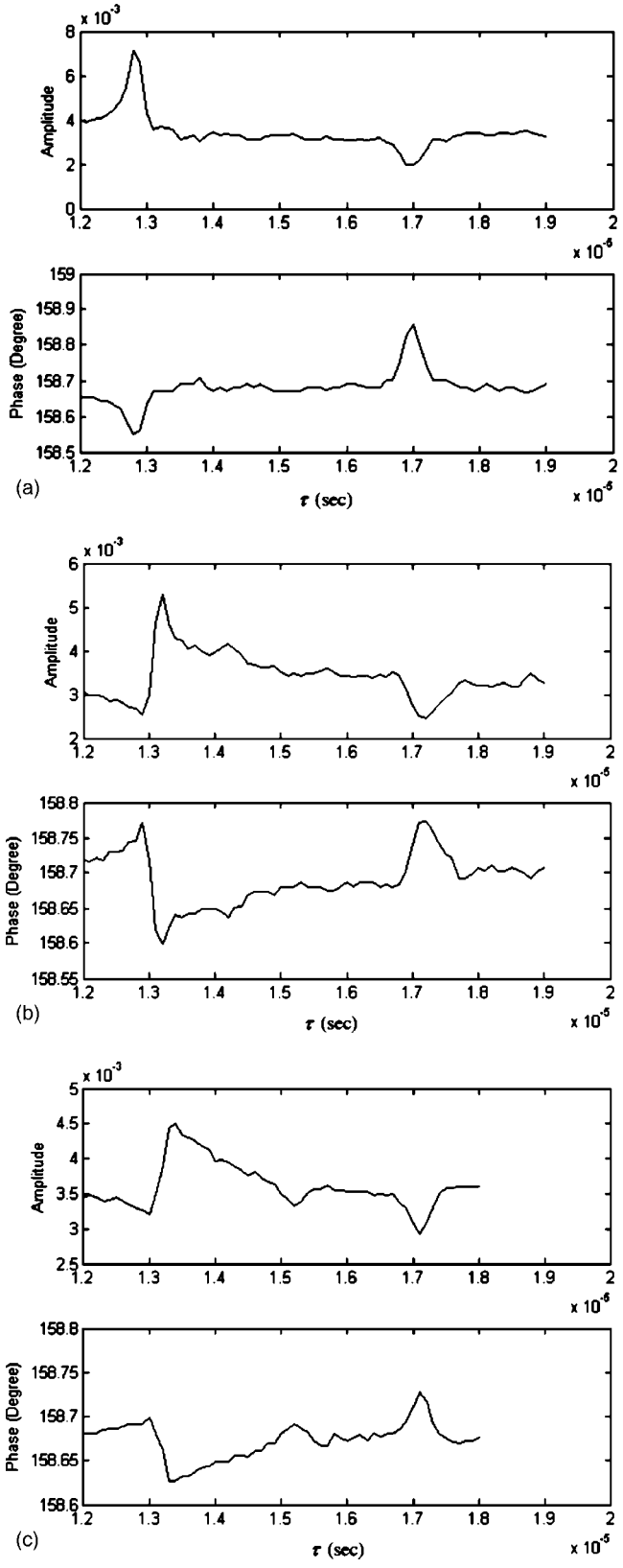

FIG. 11. Single-point scans of 3-mm-thick solid phantoms using the PTA chirp heterodyne scanning system. The optical absorption and scattering coefficients of the phantoms are (a) $\mu_a = 9\ \mathrm{cm}^{-1}$ and $\mu_s' = 2\ \mathrm{cm}^{-1}$; (b) $\mu_a = 7\ \mathrm{cm}^{-1}$ and $\mu_s' = 1.2\ \mathrm{cm}^{-1}$; (c) $\mu_a = 3\ \mathrm{cm}^{-1}$ and $\mu_s' = 0.15\ \mathrm{cm}^{-1}$.

surface reflections are clearly visible in both amplitude and phase traces. The generation of peaks or troughs is determined by the acoustic impedance at the fluid–solid boundary. For the solid phantoms, the density was measured to be 1160 kg/m^3. The sound velocity, c_s, was 1550 m/s, which was measured using the time-of-flight technique. (C) For samples with optical absorption depths commensurate with their thickness, as shown in Fig. 11(c), an additional trough is generated halfway between reflections of the incident acoustic wave at the front and back surface, corresponding to direct absorption at the back interface and launching of an acoustic pulse traveling toward the front surface (transducer location).

V. CONCLUSIONS

A linear frequency-domain PTA theory has been developed for a composite liquid–solid–liquid one-dimensional geometry which includes acoustic attenuation effects and natural mixed (rigid and free) boundary conditions at the solid–liquid interface.[19] Numerical simulations have been carried out to study the effects of varying sample thickness and optical absorption coefficients on the PTA field. The theory was then applied to the case of a 1.8-mm-thick rubber sample immersed in water. The simulated PTA field was compared with the experimental results obtained from a frequency scan system. The results display the following trends: (1) The amplitude of the pressure field contains acoustic standing-wave patterns. (2) For an opaque solid, the interference pattern is mainly determined by the thickness of the solid. For a translucent solid, it is strongly dependent on the optical absorption coefficient. (3) The frequency values of the minima or maxima contained in the measured frequency scan results can be used to measure the acoustic speed and the optical absorption coefficient of the experimental system. For the tested black-rubber/water system, the measured acoustic speed is 1800 m/s, which is within the range reported in the literature.[22]

A heterodyned lock-in PTA imaging technique using an intensity-modulated frequency-swept (chirped) laser beam was also developed as an extension of the single-frequency PTA setup. Compared to the single-frequency scan system, the PTA chirp scan method has significant advantages of precise depth localization, fast scanning speed, and high signal-to-noise ratio. This lock-in system can be used to perform subsurface slice-by-slice two-channel (amplitude and phase) imaging from operator determined, precisely controlled depths, thus improving the reliability and signal-to-noise ratio (i.e., dynamic range) of photoacoustic imaging over conventional pulsed laser detection. Good agreement was obtained between the numerical and experimental results on a flat, 5.4-mm-thick rubber sample and a rubber specimen with curved top surface. Experiments were also carried out on solid tissue phantoms with different optical absorption and scattering coefficients, indicating that the PTA depth profilometry system using a continuous-wave laser source and frequency-swept, heterodyned detection may be applicable in a biomedical imaging setting.

ACKNOWLEDGMENTS

The authors wish to acknowledge a CHRP Grant from the Natural Sciences and Engineering Research Council of Canada (NSERC) which made this research possible. We also wish to thank Professor William Whelan, Ryerson University, for his valuable advice on this project.

[1] A. C. Boccara and D. Fournier, ''Principles and perspectives of photothermal and photoacoustic phenomena—historical perspectives,'' in *Progress in Photothermal and Photoacoustic Science and Technology*, edited by A. Mandelis (North-Holland, New York, 1992), 4–30.

[2] K. P. Koestli, M. Frenz, H. P. Weber, G. Paltauf, and H. Schmidt-Kloiber, ''Pulsed optoaoustic tomography of soft tissue with a piezoelectric ring sensor,'' *Biomedical Optoacoustics*, edited by A. A. Oraevsky, Proc. SPIE Vol. 3916, 67-74 (Bellingham, WA, 2000).

[3] A. A. Oraevsky, A. A. Karabutov, S. V. Solomatin, E. V. Savateeva, V. G. Andreev, Z. Gatalica, H. Singh, and R. D. Fleming, ''Laser optoacoustic imaging of breast cancer *in vivo*,'' *Biomedical Optoacoustics II*, Proc. SPIE Vol. 4256, 6–15 (A. A. Oraevsky, Ed., Bellingham, WA, 2001).

[4] M. Eghtedari, M. Motamedi, V. L. Popov, N. A. Kotov, and A. A. Oraevsky ''Optoacoustic imaging of gold nanoparticles targeted to breast cancer cells,'' *Biomedical Optoacoustics*, Proc. SPIE Vol. 5320, 21–28 (A. A. Oraevsky, Ed., Bellingham, WA, 2004).

[5] H. Hogan, ''Photonics sounds off,'' in Biophotonics International, Vol. 7, 40–45 (September/October 2000).

[6] V. G. Andreev, A. A. Karabutov, S. V. Solomatin, E. V. Savateeva, V. Aleynikov, Y. Z. Zhulina, R. D. Fleming, and A. A. Oraevsky, ''Optoacoustic tomography of breast cancer with arc-array transducers,'' in *Biomedical Optoacoustics*, Proc. SPIE Vol. 3916, 36–47 (A. A. Oraevsky, Ed., Bellingham, WA, 2000).

[7] C. G. A. Hoelen, R. G. M. Kolkman, M. Letteboer, R. Berendsen, and F. F. de Mul, ''Photoacoustic tissue scanning (PATS),'' in *Optical Tomography and Spectroscopy of Tissue III*, Proc. SPIE Vol. 3597, 336–343 (1999).

[8] P. C. Beard and T. N. Mills, ''An optical detection system for biomedical photoacoustic imaging,'' *Biomedical Optoacoustics*, Proc. SPIE Vol. 3916, 100–109 (A. A. Oraevsky, Ed., Bellingham, WA, 2000).

[9] P. M. Henrichs, J. Meador, K. Mehta, T. Miller, A. Yee, and A. A. Oraevsky, ''Phantoms for development of LOIS as a modality for diagnostic imaging of breast cancer,'' *Biomedical Optoacoustics*, Proc. SPIE Vol. 5320, 8–15 (A. A. Oraevsky, Ed., Bellingham, WA, 2004).

[10] G. Ku, X. Wang, X. Xie, G. Stoica, and L. H. Wang, ''Photoacoustic tomography of rat brain *in vivo* using multibandwidth ultrasonic detection,'' *Biomedical Optoacoustics*, Proc. SPIE Vol. 5320, 172–178 (A. A. Oraevsky, Ed., Bellingham, WA, 2004).

[11] A. A. Karabutov, N. B. Podymova, and V. S. Letokhov, ''Time-resolved optoacoustic measurement of absorption of light by inhomogeneous media,'' Appl. Opt. **34**, 1484–1487 (1995).

[12] A. Mandelis, ''Signal-to-noise ratios in lock-in amplifier synchronous detection: A generalized communications systems approach with application to frequency-, time-, and hybrid (rate-window) photothermal measurements,'' Rev. Sci. Instrum. **65**, 3309–3323 (1994).

[13] A. Oraevsky and A. Karabutov, ''Ultimate sensitivity of time-resolved opto-acoustic detection,'' *Biomedical Optoacoustics*, Proc. SPIE Vol. 3916, 228–239 (A. A. Oraevsky, Ed., Bellingham, WA, 2000).

[14] D. Fournier, F. Charbonnier, and A. C. Boccara, ''Method and device for multichannel analysis detection,'' French Patent 2666 (1993).

[15] J. Selb, S. Leveque-Fort, L. Pottier, and C. Boccara, ''Setup for simultaneous imaging of optical and acoustic contrasts in biological tissues,'' *Biomedical Optoacoustics II*, Proc. SPIE Vol. 4256, 200–207 (A. A. Oraevsky, Ed., Bellingham, WA, 2001).

[16] A. Mandelis and C. Feng, ''Frequency-domain theory of laser infrared photothermal radiometric detection of thermal waves generated by diffuse-photon-density wave fields in turbid media,'' Phys. Rev. E **65**, 021909–021909 (2002).

[17] L. Nicolaides, Y. Chen, A. Mandelis, and I. A. Vitkin, ''Theoretical, experimental, and computational aspects of optical property determination of turbid media using frequency-domain laser infrared photothermal radiometry,'' J. Opt. Soc. Am. A **18(10)**, 2548–2556 (2001).

[18] A. Karabutov and V. Gusev, *Laser Optoacoustics* (AIP, New York, 1993).

[19] A. Mandelis, N. Baddour, Y. Cai, and R. Walmsley, ''Laser induced linear photo-thermo-acoustic pressure-wave pulses in water,'' *J. Opt. Soc. Am.* (submitted).

[20] D. R. Lide, *CRC Handbook of Chemistry and Physics* (CRC, Boca Raton, FL), pp. 14–38.

[21] D. P. Almond and P. M. Patel, *Photothermal Science and Techniques* (Chapman and Hall, London, 1996), pp. 16–17.

[22] J. Krautkramer and H. Krautkramer, *Ultrasonic Testing of Materials*, 3rd ed. (Springer, Berlin, 1983).

[23] N. Bilaniuk and G. S. K. Wong, ''Speed of sound in pure water as a function of temperature,'' J. Acoust. Soc. Am. **93**, 1609–1612 (1993).

[24] A. Rosencwaig and A. Gersho, ''The photoacoustic effect with solids,'' J. Appl. Phys. **47**, 64–69 (1976).

[25] R. C. Hayser, ''Acoustical measurements by time delay spectrometry,'' J. Audio Eng. Soc. **15**, 370–379 (1967).

[26] R. C. Hayser, ''Determination of loudspeaker signal arrival times I,'' J. Audio Eng. Soc. **19**, 734–741 (1971).

[27] M. C. Pilatou, R. G. M. Kolkman, E. Hondebrink, R. Berendsen, F. F. M. DeMul, ''Photo-acoustic Imaging of Microvascular Structure in Tissue,'' *Biomedical Optoacoustics*, Proc. SPIE Vol. 3916, 48–54 (A. A. Oraevsky, Ed., Bellingham, WA, 2000).

[28] D. D. Royston, ''Optical properties of scattering and absorption materials used in the development of optical phantoms at 1064 nm,'' J. Biomed. Opt. **1**, 110–116 (1996).